https://doi.org/10.5194/amt-2024-106
Preprint. Discussion started: 12 July 2024

Atmospheric Measurement Techniques
Discussions

An introduction of Three-Dimensional Precipitation Particles Imager (3D-PPI)

Jiayi Shi[1], Xichuan Liu[1,2], Lei Liu[1,2], Liying Liu[3], Peng Wang[3]

[1]College of Meteorology and Oceanography, National University of Defense Technology, Changsha, China
[2]High Impact Weather Key Laboratory of CMA, Changsha, China
[3]Aerospace NewSky Technology Co., Ltd, Wuxi, China

Correspondence: Xichuan Liu (liuxichuan17@nudt.edu.cn)

Abstract. A Three-Dimensional Precipitation Particles Imager (3D-PPI) is presented as a new instrument for measuring the size, fall velocity, and three-dimensional shape of the precipitation particles. The 3D-PPI consists of three high-resolution cameras with telecentric lenses and one high-speed camera with one non-telecentric lens. The former records the high-resolution images of falling particles from three angles, based on which the three-dimensional shapes of particles can be restored by using a 3D reconstruction algorithm, and the observation volume is large enough to obtain the particle size distribution (PSD). The latter records the images of the falling precipitation particles with 200 frames per second, based on which the falling velocity of particles can be calculated. The field experiment of the 3D-PPI and OTT PARSIVEL disdrometer (OTT) was conducted at Tulihe, China, more than 880,000 snowflakes were recorded during a typical snowfall case lasting for 13 hours, and the results show that the PSD obtained by the 3D-PPI and OTT a good agreement. It shows a potential application in atmospheric science, polar research, and other fields.

1 Introduction

Precipitation microphysics refers to the interactions and processes associated with the scale of individual precipitation particles. Microphysics and microstructure, i.e. the distribution of particle properties such as size, shape, density, and mass, together determine the state and evolution of clouds and precipitation at this scale and are intrinsic to the process of cloud and precipitation evolution (Taylor, 1998). The microphysical properties of spherical or ellipsoidal raindrops have been relatively well studied. Research on ice-phase precipitation (such as snowflakes) microphysics is complicated by the complex geometry of individual snowflakes. Minor variations in the air temperature and humidity can cause significant changes in the shape of ice crystals, resulting in a wide variety of crystal shapes ranging from simple plates and columns to complex dendrites or needles (Bailey and Hallett, 2012). Aggregation combines individual crystals into complex and random shapes of snowflakes. Despite the challenges associated with measuring snowflake shapes, the significance of this work is substantial. The accurate measurement of snowflake shapes is paramount for advancing our understanding of atmospheric sciences, including the formation of ice and mixed-phase clouds, as well as precipitation processes (Morrison et al., 2020).   Specifically, accurate snowflake shapes are critical for triple-frequency radar retrievals, as they directly influence the interpretation of radar echoes and the assessment of snow's microphysical properties (Mason et al., 2019). Besides, precise shape descriptions of snowflakes will significantly improve the radar-based quantitative winter precipitation estimation (Notaroš et al., 2016).

The absence of accurate information on the 3D shape of precipitation particles leads to errors in the parameterization of physical processes in cloud precipitation and quantitative precipitation estimation (QPE) using weather radar. The assumption that true snowflakes are ellipsoidal may lead to inaccurate scattering matrix calculations, and hence incorrect determination of snow water equivalent (Tyynelä et al., 2011). The use of the ellipsoid approximation is only valid for smaller particles, and shape properties play an increasingly important role in scattering calculations as the snowflake scale increases (Olson et al., 2016). Between isovolumetric spheres and hexagonal columns, more accurate snowflake models are needed. In addition, an assessment of the sensitivity of high-frequency falling snow characteristics using an idealized simulated snowflake model indicates the necessity for a scattering database of snowflakes, in which the highly variable shapes should be taken into consideration (Kneifel et al., 2010). Ideal ice crystal models were created in the form of dendritic, thin plate, stellar plate, crown prism, and hollow column, and the scattering effects of these geometries were calculated using the Discrete Dipole Approximation (DDA) approach (Kim, 2006). The results indicate that the scattering characteristics of these ideal snowflakes are highly sensitive to their shapes. This further emphasizes the necessity for accurate shape modeling (Kim et al., 2007).

Different in-situ instruments were invented to measure the precipitation particles. The OTT PARSIVEL disdrometer (Loffler-Mang and Joss, 2000) can obtain the horizontal size (fall velocity) of particles according to the decrease (duration) of laser signal by attenuation. However, the one-dimensional measurement concept requires additional assumptions to correctly size irregularly shaped particles such as snowflakes (Battaglia et al., 2010), the shape of particles cannot be obtained. The Two-Dimensional Video Disdrometer (2DVD) can obtain the three-dimension particle shape by using two line-scan cameras with an angle of 90°, the sampling area is 10×10 cm^2 (Bernauer et al., 2016). It should be noted that particle shape estimates may still be subject to bias due to horizontal winds (Helms et al., 2022). The Multi-angle Snowflake Imager (MSI) can obtain the three-dimensional shape and fall velocity of individual snowflakes by using four line-scan cameras with an angle of 45°, a limitation lies in its restricted sampling area, allowing the measurement of only one snowflake within a narrow field of view (Minda et al., 2017).

In addition to line-scan cameras, several planar camera instruments have been developed. The Snowfall Video Imager (SVI) employs a camera and a light source to record images of snowflakes in free fall, and its subsequent evolution, the Precipitation Imaging Package (PIP), employs advanced digital image processing algorithms to enhance the precision and resolution of snowflake imaging (Newman et al., 2009; Pettersen et al., 2020a). The Precipitation Imaging Package (PIP) provides physically consistent estimates of snowfall intensity and volume equivalent densities from high-speed images, although its equivalent density parameterization requires further refinement for extremely high snow-to-liquid ratio snowfall events (Pettersen et al., 2020b). The video precipitation sensor (VPS) can obtain the shape and fall velocity of hydrometeors when the particles fall through the sampling volume, the camera is exposed twice in a single frame, which allows the double exposure of particle images to be recorded, and the size and fall velocity of particles can obtained simultaneously (Liu et al., 2014; Liu et al., 2019). The Video In-situ Snowfall Sensor (VISSS) consists of two cameras with LED backlights and telecentric lenses, it can measure the shape and size of snowflakes in a large observation volume with high pixel resolution (43 to 59 μm·px^{-1}) (Maahn et al., 2024). Nevertheless, it is challenging to resolve highly fine structures of snowflakes with only two angles of observation.

The Multi-Angle Snowflake Camera (MASC) simultaneously captures three high-resolution (30 μm·px^{-1}) images of falling hydrometeors from three different viewpoints (Garrett et al., 2012), which provides the conceptual possibility of 3D reconstruction of the observed snowflakes. The Visual Hull (VH) algorithm was used to reconstruct the 3D shape of snowflakes through multi-angle imaging, and the addition of two more cameras to MASC has been shown to improve reconstruction results (Kleinkort et al., 2017). Nevertheless, only 10^2–10^4 particles were observed during a typical snowfall event (Gergely and Garrett, 2016), which is insufficient to permit the reliable estimation of the particle size distribution (PSD) (Gergely and Garrett, 2016).

Currently, instruments are needed that not only provide a finer 3D structure of the snowflake but also capture enough particles per unit time to estimate the PSD. This study presents a new instrument: Three-Dimensional Precipitation Particle Imager (3D-PPI), the instrument design and main components are introduced in Sec.2, the calibration of the camera and image binarization are described in Sec.3, and detailed algorithms including image processing, particle matching, particle localization, and 3D reconstruction are presented in Sec.4, the preliminary results of field experiment are discussed in Sec.5, The last part summarizes the main results and future work of 3D-PPI.

2 Instrument design

The 3D-PPI contains three high-resolution cameras with telecentric lenses (numbered Cam0, Cam1 and Cam2 in this paper) and one high-speed camera with a non-telecentric lens (numbered Cam3), four high-brightness LED arrays are used as light sources to illuminate the observation volume, and a ZYNQ driver circuit is developed to control the cameras, and light source, transmit the raw images to the PC terminal. To improve the instrument's working efficiency, a capacitive rain sensor is adopted as a trigger, the cameras only work when the precipitation occurs. The concept drawing, prototype and snowflake images of 3D-PPI are shown in Fig. 1.

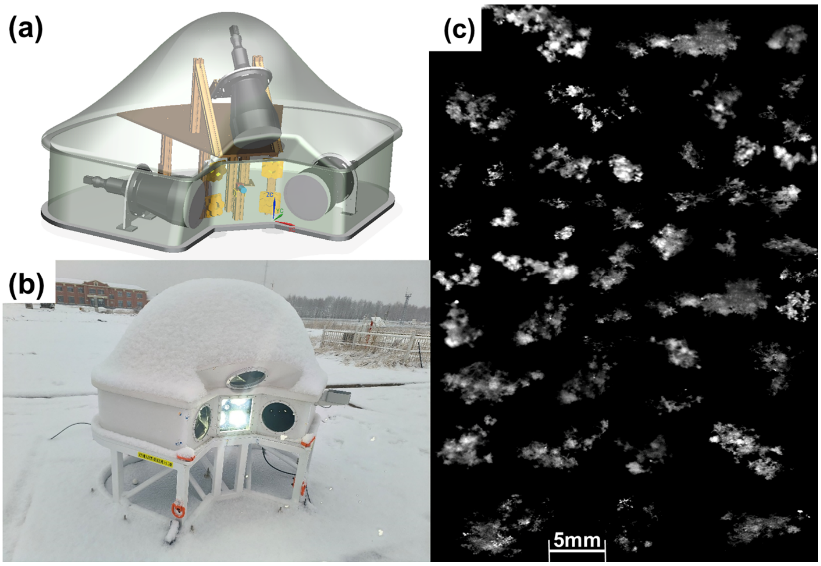

Figure 1. (a) Concept drawing of the 3D-PPI. **(b)** The prototype 3D-PPI deployed at Tulihe, China., (photo by J. Y. Shi). **(c)** Randomly selected snowflakes were observed on 6 April 2024 between 0453 UTC and 11:13 UTC.

The high-resolution camera is a Sony IMX304 with a resolution of 4096 × 3000 and a frame rate of 5 fps. The high-speed camera is a Sony IMX287 with a resolution of 720 × 540 and a frame rate of 200 fps. The detailed technical parameters are shown in Table 1.

Table 1: Technical specifications of the cameras.

	High-resolution camera	High-speed camera
Type	CMOS, Global shutter	CMOS, Global shutter
Model	Sony IMX304	Sony IMX287
Pixel resolution [μm px^{-1}]	3.45 ×3.45	6.9 ×6.9
Frame size used [px]	4096×3000	720×540
Frame rate [Hz]	5	200
Effective exposure time [μs]	20	20

The high-speed camera is positioned horizontally at the center, while the three high-resolution cameras are oriented at a 45° angle relative to the optical axis of the high-speed camera. The high-brightness LED array light sources are situated on the same side as the cameras, with the overlapping region of the LED lighting beams serving as the observation volume. The observation volume is an irregular region intersected by three rectangular light columns all with a cross-sectional area size of 17cm × 12.5cm and an observation volume size of 1505.327cm^3. When particles are present in this observation volume, the light reflected and scattered by the particles passes through the lenses, creating a projected image on the cameras, as illustrated in Fig. 2.

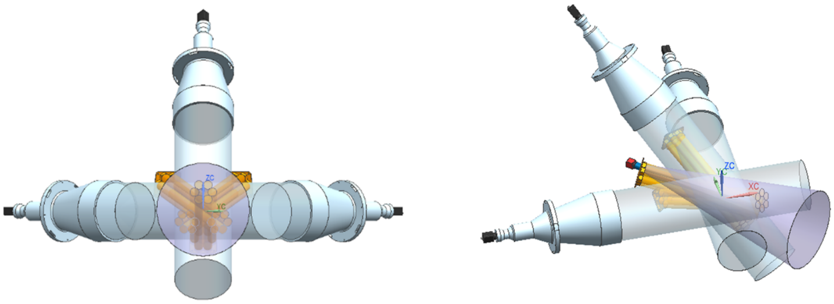

Figure 2. Optical structure of 3D-PPI

For the telecentric lens, the magnification is 0.083, the aperture is F6.5, single pixel size is 0.042mm for the high-resolution camera. This configuration yields a field of view measuring 170mm×125mm, a depth of field of 104.3mm, and an optical distortion of 0.044%. For the non-telecentric lens, the focal length is 12mm, the aperture ranges from F2.4 to F16, and the magnification is 0.026 at a working distance of 450mm. A single pixel size is 0.265mm for a high-speed camera, and the field of view is 191mm×143mm. The optical distortion is 0.16% at minimal.

The utilization of telecentric lenses eliminates the sizing error caused by the uncertain distance between the snowflakes and the cameras. Unlike non-telecentric lenses, telecentric lenses are based on the principle of parallel light imaging, resulting in identical objects at different distances from the lens having the same size in the image (Fig. 3a, c), which leads to a difference in the method of performing 3D reconstruction later in Sec. 4 (Fig. 3b, d). With an optical distortion of 0.044%, the telecentric lens effectively minimizes distortion, establishing a linear correspondence between image coordinates and world coordinates. This alignment greatly simplifies camera calibration, it will be elaborated upon in Sec. 3.

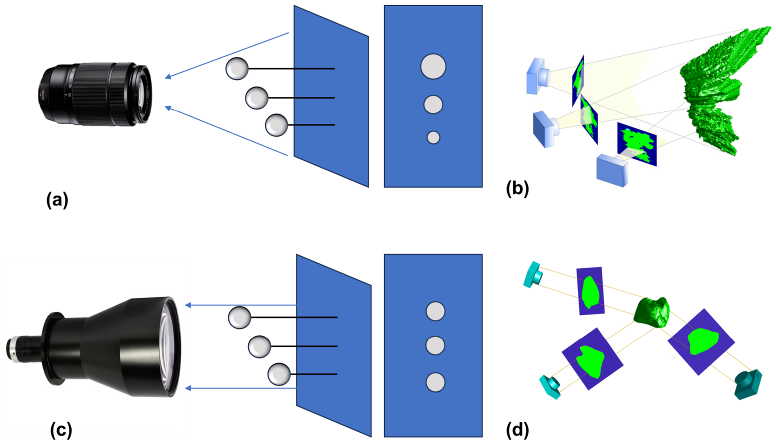

Figure 3. Illustration of imaging characteristics and reconstruction of a snowflake using three cameras. **(a)** non-telecentric lens imaging characteristics; **(b)** non-telecentric lenses back-projected to obtain three visual cones (Kleinkort et al., 2017); **(c)** telecentric lens imaging characteristics; **(d)** telecentric lenses back-projection to three visual columns.

3D-PPI has 4 light source arrays, each consisting of 6 high brightness LEDs organized into a cluster to create an array lighting system. Each LED is 5W with a total power of 120W. This LED lighting system integrates a high-brightness LED chip, substrate, heat sink, casing, leads, protective features, and other functionalities into a single unit. At its core lies the LED chip, utilizing white high-brightness LED chips. Each LED is equipped with a converging lens, facilitating the creation of a cone-shaped beam of light. The design and physical representation of the LED array lighting system is illustrated in Fig. 4. The LED light sources are arranged in a parallel configuration, leading to a unidirectional power supply interface. The LED operates in either constant current mode or trigger mode, with the former ensuring a consistent light output, thereby enhancing the uniformity of illumination within the observation volume.

Figure 4. (a) LED array lighting group design; **(b)** Physical picture; **(c)** Cone-shaped beam formed by LED array lighting group.

3 Calibration

3.1 Calibration of cameras

Camera calibration is the basis for obtaining three-dimensional spatial information from two-dimensional images. There is a one-to-one correspondence between the spatial scene points and their image points in the image, and their positional relationship is determined by the camera imaging geometric model (Cheng and Huang, 2023). The parameters of this geometric model are called camera parameters, which can be determined by experiment and computation, and the process of solving the parameters experimentally and computationally is called camera calibration. The purpose of camera calibration in this section is to estimate the projection matrix KM_i of the transformation relationship between the 3D spatial points and each pixel plane pixel point in the world coordinate system. The geometric model for telecentric lens imaging is described in detail in Appendix A.

Since the chessboard grid (Fig. 5b) has an ideal regularity and is easy to be recognized, it is used here as a calibration plate for camera calibration, and the apparent 3D coordinate point to the image pixel coordinate point is a linear change without considering the camera/lens distortion. The equation obtained by deriving the telecentric lens imaging model is as follows:

$$\begin{bmatrix} \frac{\beta}{S_v}r_{11} & \frac{\beta}{S_v}r_{12} & \frac{\beta}{S_u}r_{13} & \frac{\beta}{S_u}t_x+u_0 \\ \frac{\beta}{S_v}r_{21} & \frac{\beta}{S_v}r_{22} & \frac{\beta}{S_v}r_{23} & \frac{\beta}{S_u}t_y+v_0 \end{bmatrix} \begin{bmatrix} X_w \\ Y_w \\ Z_w \\ 1 \end{bmatrix} = \begin{bmatrix} u \\ v \end{bmatrix} \tag{1}$$

where β is the telecentric camera magnification; S_u and S_v are the length and width dimensions of the individual image; r_{ij} and t_x (t_y) denote the matrix elements of the rotation and translation process from the world coordinate system (WCS) to the camera coordinate system (CCS) respectively, and these parameters relate solely to the relative position of the cameras; and u_0 and v_0 are the horizontal and vertical coordinates of the camera's main point offsets, which may change over time.

The coordinate points (X_w, Y_w, Z_w) in WCS are projected to the coordinate points (u,v) in the pixel coordinate system (PCS) through the 2 × 4 matrix (also denoted as KM) on the left side of Eq. (1). In particular, the three telecentric lenses are in the same WCS, and each lens corresponds to a projection parameter KM_i (i=1,2,3).

To obtain the projection parameters, the following steps are executed: Firstly, establish the position of the world coordinate system by capturing images of a 3D checkerboard grid from the same localization using three cameras. Secondly, measure the precise coordinates of all checkerboard corners in the world coordinate system (X_{wj}, Y_{wj}, Z_{wj}) (j denotes the number of corner points), and identify the pixel coordinates (u_{ij}, v_{ij}) of these corners in the ith images. Thirdly, formulate super-determined linear equations, such as Eq. (2), and estimate the projection matrix for each camera optimally using the least squares method.

$$KM_i \cdot \begin{bmatrix} X_{w1} & X_{w2} & \cdots & X_{wj} \\ Y_{w1} & Y_{w2} & \cdots & Y_{wj} \\ Z_{w1} & Z_{w2} & \cdots & Z_{wj} \\ 1 & 1 & \cdots & 1 \end{bmatrix} = \begin{bmatrix} u_{i1} & u_{i2} & \cdots & u_{ij} \\ v_{i1} & v_{i2} & \cdots & v_{ij} \end{bmatrix} \tag{2}$$

Where i=1,2,3, and j has a maximum value of 264, the value is determined based on the number of corner points captured by each camera.

It is important to note that the three-dimensional checkerboard plays an irreplaceable role in this calibration procedure, it cannot be replaced by a normal two-dimensional checkerboard. The projection matrix cannot be obtained by using only a 2D checkerboard for the following reasons. In the world coordinate system established by a single two-dimensional checkerboard, the super-deterministic linear Eq. (2) is established in the same way as in the previous method, but then the values of all three-dimensional world coordinate points are the same so that the matrix $A = \begin{bmatrix} X_{w1} & X_{w2} & \cdots & X_{wj} \\ Y_{w1} & Y_{w2} & \cdots & Y_{wj} \\ Z_{w1} & Z_{w2} & \cdots & Z_{wj} \\ 1 & 1 & \cdots & 1 \end{bmatrix}$. The third and fourth-row values are the same, then linear correlation, in the process of solving by least squares to calculate the pseudo-inverse matrix of A. If the third and fourth rows of A are linearly correlated, the determinant of A is 0, that is, it is a singular matrix, which is impossible to inverse, leading to errors in the process of solving by least squares, and therefore the planar two-dimensional checkerboard grid cannot be realized to solve the calibration.

The two mutually perpendicular three-dimensional checkerboard planes of the three-dimensional checkerboard grid define a common world coordinate system (WCS) (Fig. 5b). The calibration results show that the average reprojection error for 3D-PPI is 0.32 pixels.

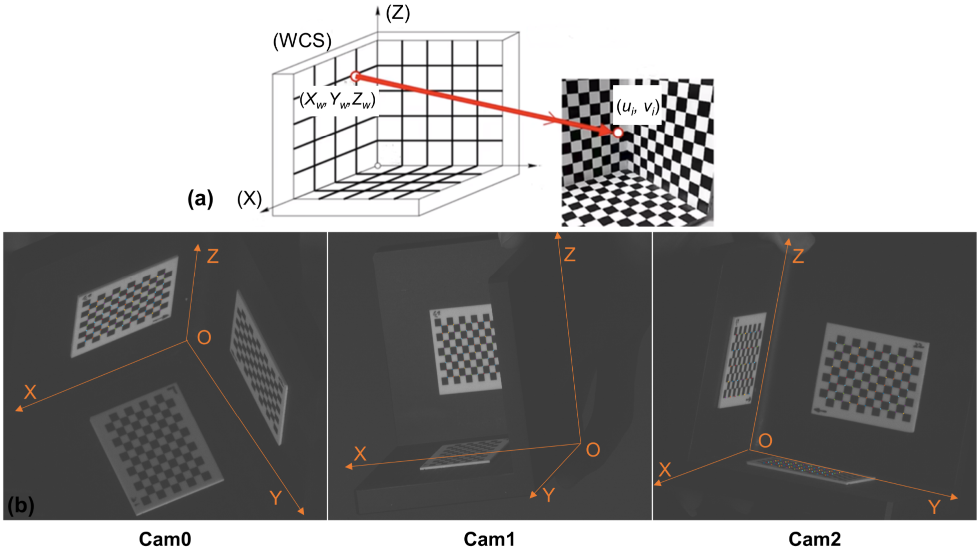

Figure 5. (a) 3D checkerboard calibration principle; **(b)** World coordinate system with three camera views.

3.2 Calibration of image binarization

Calibration is required to convert D_{max} and D_{eq} from pixels to micrometers (D_{max} is the distance between the two largest points of the particle profile, and D_{eq} is the diameter of the circle equal to the area of the particle profile). The calibration process utilizes reference ceramic spheres with absolute sphericity ranging from 1 to 25 millimeters in diameter, which are dropped into the observation volume of 3D-PPI (Fig. 6a). The materials of spheres have a similar refractive index to the snowflakes. The image of each diameter sphere is optimally binarized manually so that the image contour is as circular as possible, at which point D_{max} and D_{eq} are almost equal. The scatterplot about the actual diameter of the spheres and the diameter of the image contour circle and the linear least-squares fit straight line plotted together (Fig. 6b), resulting in

$$D_{\max}[px] = (24.0509 \pm 0.0003) \cdot D_{\max}[\mu m] - 0.5473 \tag{3}$$

for Cam0 (Fig. 6a), and

$$D_{\max}[px] = (24.3838 \pm 0.0006) \cdot D_{\max}[\mu m] - 3.8484 \tag{4}$$

for Cam1,

$$D_{\max}[px] = (24.3710 \pm 0.0005) \cdot D_{\max}[\mu m] - 1.9839 \tag{5}$$

for Cam2.

https://doi.org/10.5194/amt-2024-106
Preprint. Discussion started: 12 July 2024

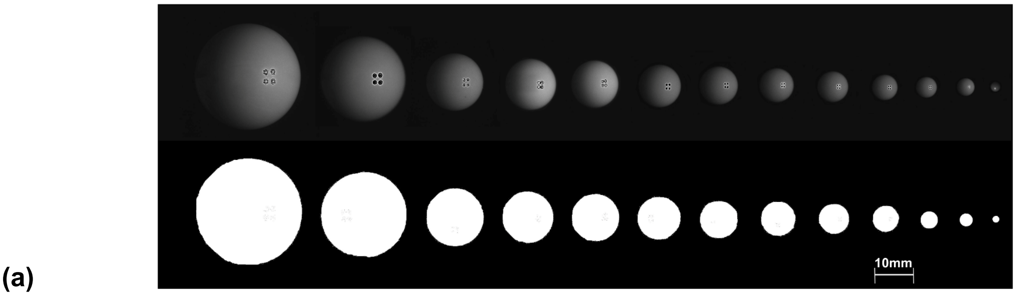

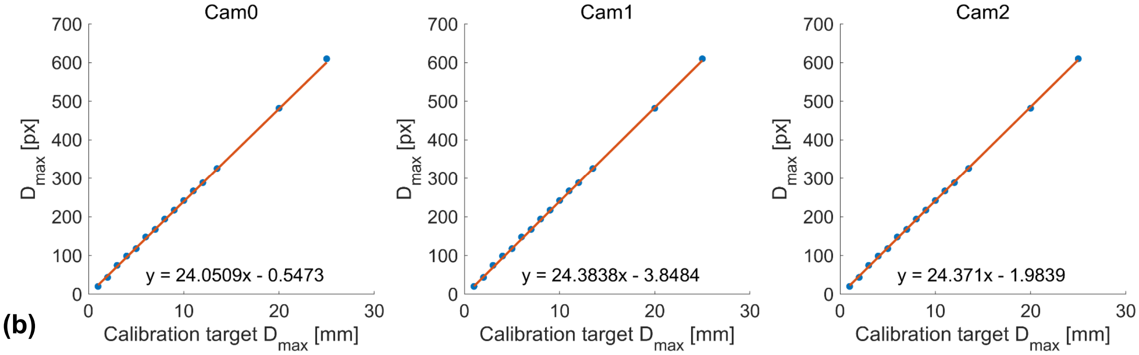

Figure 6. **(a)** The reference ceramic spheres with absolute sphericity ranging from 1 to 25 millimeters in diameter and the binarized images of each sphere; **(b)** Calibration of D_{max}, using ceramic spheres from 1 to 25mm in diameter for three high-resolution cameras (Cam0, Cam1, Cam2). The results of the linear least squares fit are also shown in the legends.

The reciprocals of the slopes of the three fitted lines are 41.5785, 41.0108, 41.0324 $\mu m \cdot px^{-1}$, and closely align with the 41.5663 $\mu m \cdot px^{-1}$ specification from the manufacturer of the high-resolution cameras. The estimated random errors from the normalized root square errors, derived from the observed and true size difference, were 1.8% (Cam0), 2.6% (Cam1), and 1.5% (Cam2) respectively, indicating that random error is negligible.

4 Algorithms

4.1 Image processing

For High-resolution camera images with the resolution of 4096×3000, no background removal and denoising are required due to low image noise and little background interference. The processing steps are as follows: (i) Image binarization. The image is binarized through adaptive thresholding. The sensitivity coefficients are determined by processing the ceramic sphere images of Section 3.2 to obtain the roundest contour, i.e., the difference between $D_{\max}$ and D_{eq} is minimized. (ii) Particles detection. Detecting connected regions in binarized images with an area greater than 20 pixels (Equivalent to 0.035 mm^2) enables the removal of small noises from the image. Snowflakes that are too small in diameter are ignored, otherwise some noise in the image will be incorrectly recognized as snowflakes. Combining into a single particle, when the centers of the

https://doi.org/10.5194/amt-2024-106
Preprint. Discussion started: 12 July 2024

connected regions are detected to be less than 4 mm apart, is necessary is an essential step. This eliminates the problem of separating the same particle into two regions in images due to the image processing method.

For the high-speed camera images with a resolution of 720×540, there is non-negligible noise and background interference, therefore, two more steps are required before image binarization and particle detection: (i) Background removal and enhancement. Background artifacts captured by high-speed cameras in natural settings can be influenced by varying lighting conditions, lens surface contamination, or other factors that change over time. To address this issue, a real-time background detection method is employed. Specifically, 1024 images are randomly selected every minute to calculate the average grayscale value, representing the minute-by-minute background changes. These background variations are then subtracted from all images taken within that minute to effectively remove the background interference. It is further necessary to enhance the contrast of the image by stretching the grey scale histogram to better distinguish between background and foreground particles. (ii) Image denoising. The median filtering is used to remove the remaining. Further, the image binarization and particle detection methods are the same as the previous high-resolution camera image processing methods.

The two types of image processing processes and the results of each step are shown in Fig. 7.

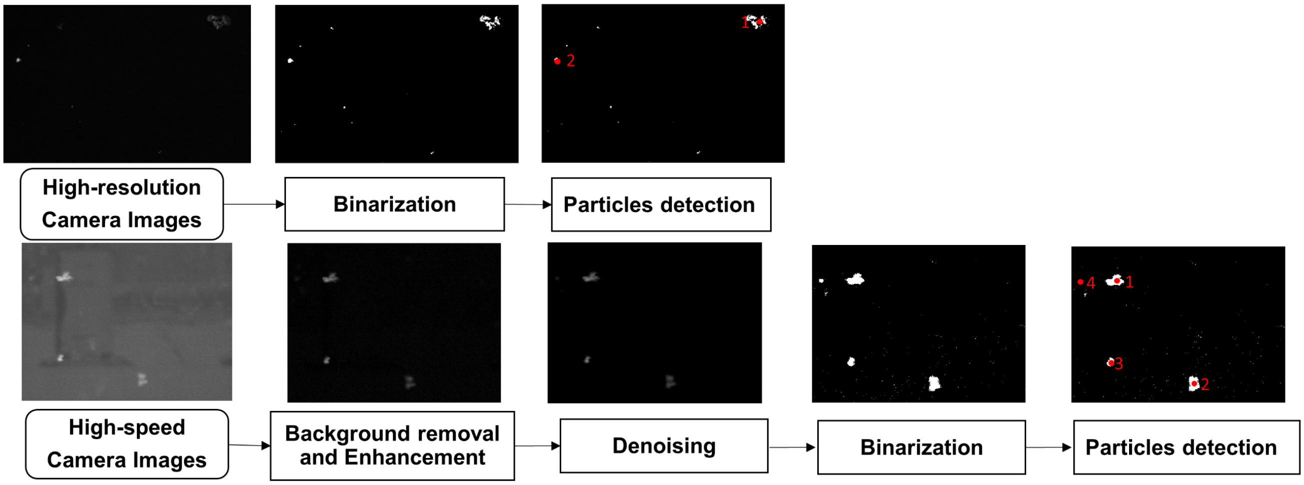

Figure 7 Flowchart of two types of image processing.

To evaluate the effectiveness of the above image processing algorithm, ceramic spheres of different diameters in section 3.2 were dropped into the observation volume, and each sphere was dropped 20 times. The measured values of D_{max} and D_{eq} are shown in Fig. 8. Overall, the measured values of D_{max} and D_{eq} agree well with the actual diameter of the ceramic spheres. The average absolute error of D_{max} measurements for all diameters of small spheres is -0.048mm, smaller spheres measurements tend to be higher than true values, larger spheres measurements tend to be lower than true values, and the average relative error is +2.2%. The average absolute error of D_{eq} measurements for all diameters of small spheres is -0.33mm, with all diameter measurements underestimating the true values by an average relative error of -2.7%. The average D_{max} tends to be higher, and the average D_{eq} tends to be lower, the sizing errors increase with the diameters of the spheres. Since the measurement errors of D_{eq} for all spherical diameters are lower than the true values, they can be utilized for systematic error correction. The higher error of the larger spheres might be caused by the uneven illumination of the larger sphere and its specular reflection.

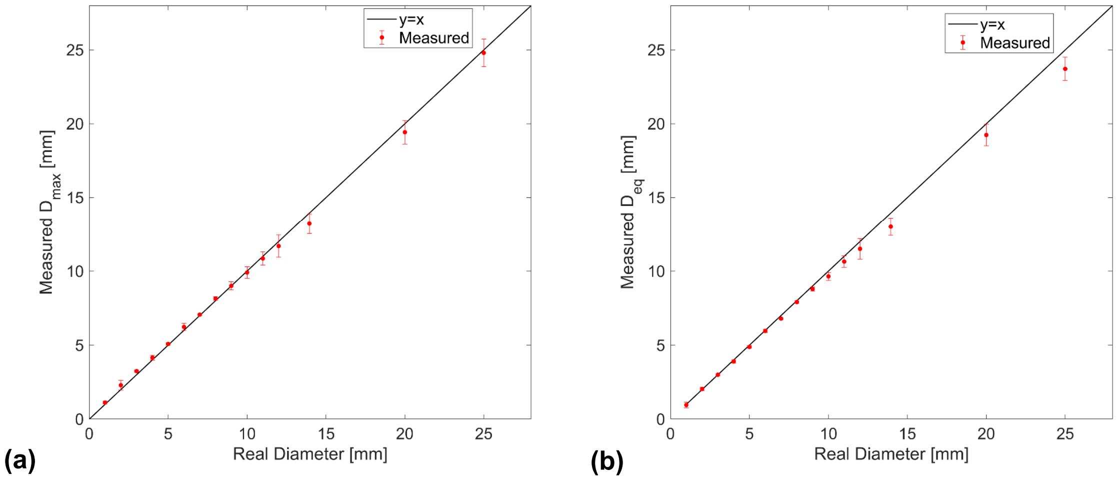

Figure 8 Measured values of D_{max} **(a)** and D_{eq} **(b)** for ceramic spheres of different diameters.

4.2 Particle matching and localization

In the observation volume of 3D-PPI, there might be numbers of particles with similar sizes, colors, shapes, and textures, which poses a challenge for particle identification from the images captured by three cameras. In this work, we propose a particle matching algorithm that addresses this issue by focusing on the spatial positions of particles in three images, as derived from the projection matrices obtained through precise calibration of the trinocular telecentric camera system. The implementation of the algorithm is detailed as follows (Fig. 9):

(i) Identify the center coordinates of each particle (P_i, *i* represents the number of recognized particles) in the image from Cam0 (Fig. 10a).

(ii) Using the projection matrix KM_1 of Cam0, *i* underdetermined linear equations corresponding to P_i are solved to obtain *i*th straight lines L_i in 3D space. L_i represents all points in three-dimensional space that can be projected onto P_i by KM_1, in other words, the lines L_i is the back-projection of the points P_i in the 3D space.

(iii) L_i lines are projected onto the planes of Cam1 and Cam2 by multiplying the projection matrices KM_1 and KM_2, resulting in *i*th line segments (Fig. 10b, c).

(iv) Identify the particles that *i*th line segments pass through, corresponding to several particles, as illustrated in Fig.10. Only if three particles can be observed on the three line segments, and each line segment intersects each of the three particles in sequence, an effective matching was achieved.

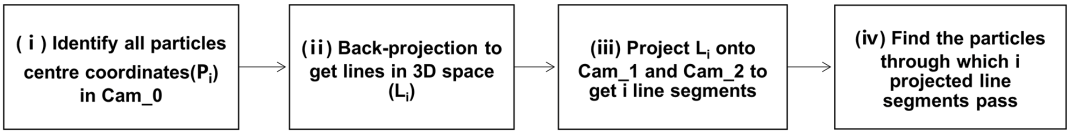

Figure 9. Flowchart of particles matching

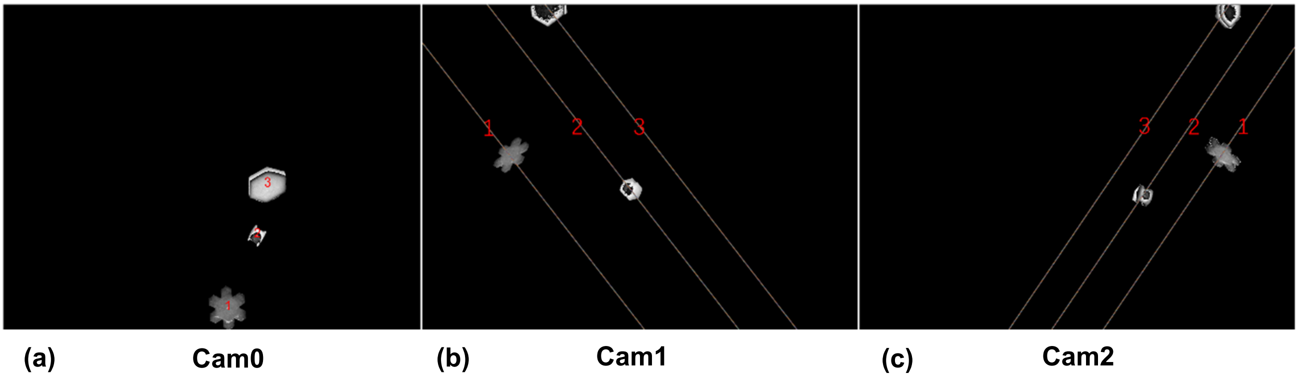

(a) Cam0 (b) Cam1 (c) Cam2

Figure 10. The three particles identified in **Cam0** can only appear on the corresponding three lines in **Cam1** and **Cam2** respectively

After completing camera calibration and particle matching, 3D reconstruction for each particle needs to be performed. The traditional process of 3D reconstruction involves dividing the entire observation volume into sufficiently fine voxel grids. However, since each particle only occupies a small space of the observation volume, traditional methods are often computationally inefficient, resulting in excessive computational resource consumption or poor reconstruction accuracy. Therefore, in consideration of these issues, we propose a method that involves preliminarily locating particles in 3D space before proceeding with subsequent 3D reconstruction, leveraging the positions of single particles in three images to identify the minimal cuboid capable of containing the particles, thereby accurately pinpointing the particles' localizations and avoiding unnecessary voxel grid searches to enhance computational efficiency.

For particles with regular geometries, back-projection of the contour centers suffices to determine the center of the 3D reconstructed object. Subsequently, the pixel size of the particle in the image can be converted to the actual size, which is then used as the length of the side of the cuboid to define the reconstruction intervals. However, precipitation particles, particularly solid ones, often exhibit highly irregular shapes. The center of the three-dimensional body projected onto the contour may not coincide with the center of the two-dimensional contour, rendering the straightforward intersection of back-projected lines inapplicable and complicating the reconstruction process.

For a single particle with irregular geometry, the pixel coordinates of the center point of the particle in Cam0, Cam1, and Cam2, respectively, have been identified and the subsequent 3D spatial localization steps are as follows:

(i) Find the back-projection line L_1 of point P_1 by KM_1. The underdetermined linear equation corresponding to P_1 is solved to obtain a straight line L_1 in 3D space. This implementation principle is similar to the second step of particle matching mentioned above.

(ii) The lines L_1 are projected onto the planes of Cam1 by multiplying the projection matrices KM_2, resulting in line segment L_2, which is represented as a 2-row by 1-column matrix.

(iii) Find the point P_2' on L_2 that is closest to P_2. Due to the irregular shape of the particle, P_2' does not necessarily coincide with P_2.

(iv) Following the same approach as in step 1, determine all lines L_3 that can be projected onto the points of P_2' in Cam1 through the projection matrix 2.

(v) Locate the 3D coordinates of the intersection of L_1 and L_3, P, which is the center of the target cuboid, and further determine the side lengths of the cuboid. From the previous steps, L_1 and L_3 are destined to intersect in 3D space, and the intersection point is regarded as the center of the rectangle, whose side lengths can be determined by converting from the pixel dimensions in the particle image to the actual physical dimensions in space.

(vi) Finally, verify that the projection of the P point through KM_3 in Cam2 is near the P_3 point and within the particle contour, otherwise, it is a failed localization.

The particle's position in space should be inside the region of the cuboid determined by localization, which will next be discretized into numerous smaller voxel grids to perform 3D reconstruction. This approach effectively overcomes the limitations associated with irregular geometries, providing a robust solution for accurate 3D reconstruction in the presence of complex particle shapes.

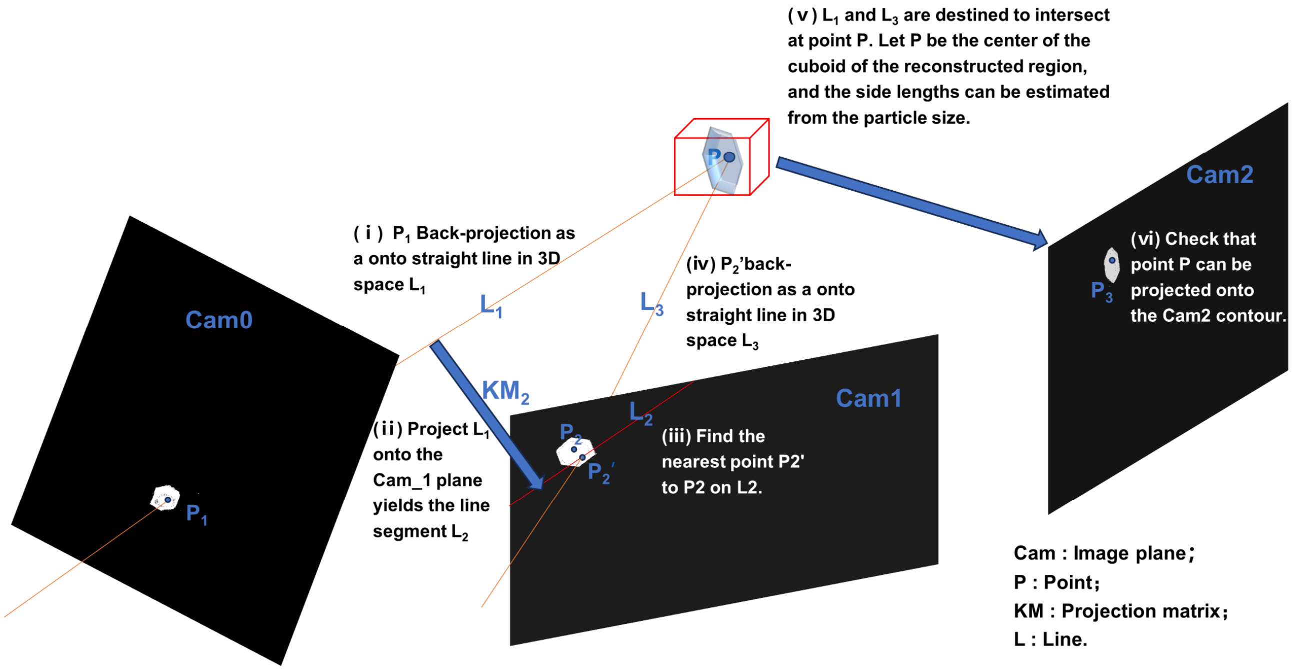

Figure 11. Steps to locate the 3D spatial position according to the image particle contours

4.3 Three-dimension (3D) reconstruction

The Visual Hull (VH) method is used to reconstruct the 3D shape of snowflakes. This approach utilizes silhouettes that have been serially calibrated using multiple viewpoints around the target, thereby enabling the reconstruction of its three-dimensional shape. A cone of silhouette is created by back-projecting the set of points of view of the previously detected silhouettes into the corresponding image planes in front of the cameras (Fig. 3b), and the intersection of these cones gives the visual hull (Hauswiesner et al., 2013). Since concave features do not affect the silhouette obtained from each image, a limitation of the visual hull method is its inability to capture concave features. Based on high-resolution contour images captured by three cameras equipped with telecentric lenses at three angles of 3D-PPI, we propose to apply the visual hull method to reconstruct the 3D shapes of snowflakes. The use of telecentric cameras allows the visual solid cones formed by back-projection to become visual solid columns (Fig. 3b, d).

The algorithm operates as follows: given a multi-viewpoint contour map and projection matrices, it ascertains whether the pixel or voxel corresponding to a spatial point on each contour map is part of the object's contour. The resulting model represents a sample of the smallest convex set that encloses the object's true shape, precluding the depiction of indentations.

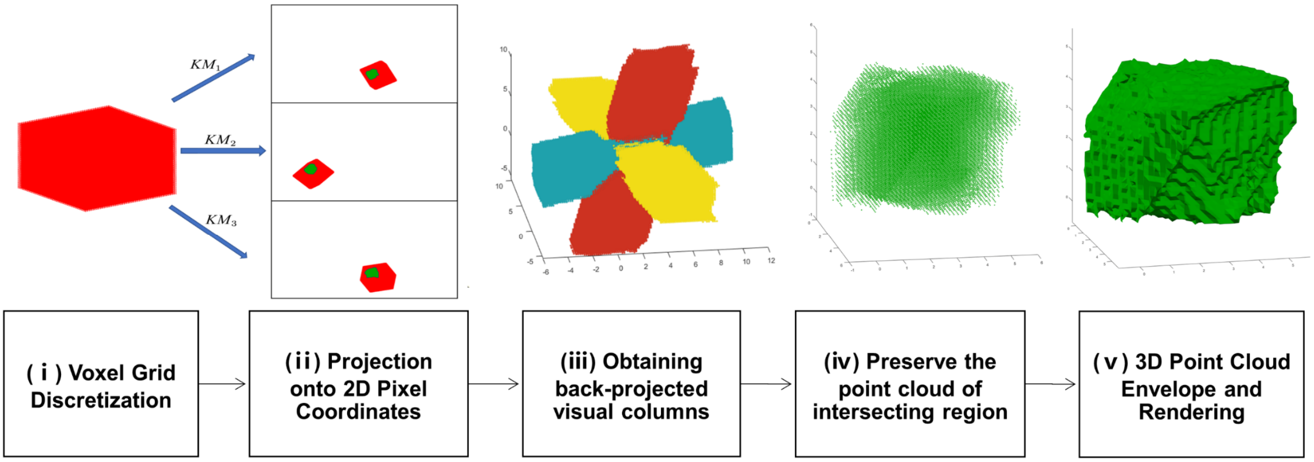

Figure 12. Flowchart of 3D construction algorithm

Initially, we employ the preliminary particle localization method described in Sec. 4 to estimate the particle's approximate spatial position. The further procedure for obtaining a 3D point cloud and reconstructing the 3D model of precipitation particles is outlined through the following refined steps (Fig. 12): (i) Voxel Grid Discretization: Subdivide the space into a voxel grid with a predefined resolution. For each voxel, extract the 3D coordinates of the upper left corner point. This grid will serve as a framework for subsequent steps. (ii) Projection onto 2D Pixel Coordinates: Utilize the projection matrix to project the 3D voxel coordinates of each voxel onto the three-angle contour, transforming them into 2D-pixel point coordinates. (iii) Obtaining back-projected visual columns (by three sets of point clouds): Mark the 3D voxel coordinates of points that can be projected onto the contours of each of the three images, that is, obtain three contours of back-projected visual columns. (iv) Preserve the point cloud of the intersecting region: Retain a point cloud within the convergence region of the three optical axes, identifying the spatial locus where the 3D reconstructed object is situated. (v) 3D Point Cloud Envelope and Rendering: Apply the triangular sectioning algorithm to extract the visual envelope of the 3D point cloud. Subsequent rendering steps will then be used to construct the 3D reconstruction model of the precipitation particle.

5 Preliminary results of field experiment

5.1 Case studies of snowfall case

To evaluate the performance of the 3D-PPI, the prototype of 3D-PPI was deployed at Tulihe, China (50.692°N, 121.652°E; 733ma.m.s.l.) from January 1st, 2024, and an OTT PARSIVEL laser disdrometer (OTT for short) was installed 10 meters apart for comparison. A typical snowfall case lasting for 13 hours, from 1900 UTC on March 28th, 2024 to 0759 UTC on March 29th, 2024 was observed and analyzed.

The PSD calculated from OTT counts is as follows (Zhang et al., 2019):

$$PSD(D_i) = \frac{1}{S \cdot T \cdot \Delta D_i} \sum_{j=1}^{32} \frac{n_{ij}}{V_j} \tag{6}$$

where PSD (D_i) ($\mathrm{mm^{-1} \cdot m^{-3}}$) is the number concentration of particles per unit volume per unit size interval ΔD_i for snowflake size D_i (mm); n_{ij} is the number of snowflakes within size bin i and velocity bin j; T (s) is the sampling time (60 s in this study), and V_j (m/s) is the falling speed for velocity bin j; S (m²) is the effective sampling area (0.18 m×0.03 m).

The PSD calculated from 3D-PPI counts is as follows:

$$PSD(D_i) = \frac{N_\mathrm{i}}{V_\mathrm{observation} \cdot N_\mathrm{ima} \cdot \Delta D_i} \tag{7}$$

Where N_i is the number of particles in the ith size bin; $V_{observation}$ (m³) is the sampling volume of the Cam0 camera, which is the product of the observation field of view and depth of field (0.17 m × 0.125 m × 0.1043 m); N_ima is the number of particles recorded during the sampling time (60 s in this study). The size descriptor D for 3D-PPI is D_{max} or D_{eq} in this paper. Considering that the sampling rate of a high-resolution camera is 5 fps, and the time for a snowflake to pass through the field of view is less than 0.2s, the probability of capturing the same snowflake in two consecutive frames is very low.

During the snowfall case, three high-resolution cameras of 3D-PPI recorded 552383 and 328792 snowflakes over two days. The PSD obtained by 3D-PPI (using two types of size descriptors) and OTT are compared (Fig. 13a, b). The PSDs measured by OTT and 3D-PPI using D_{eq} as a size descriptor are highly consistent, however, they deviate significantly from those using D_{max} as a size descriptor. PSDs are described by D_{max} as opposed to D_{eq} across a larger range of sizes, and it may be more valuable to describe them with D_{eq}. The peaks of D_{eq} were all near 0.4 mm and varied very little over the days. There were more and more concentrated small particles on March 28 compared to March 29 (Fig. 13a), and the average particle size was consistently smaller (Fig. 13e).

The trends of the number density of particles observed by the two instruments were similar, the correlation coefficients are 0.94 and 0.96 for the two days. Comparison of temporal plots, some periods (19:00 to 19:50, 20:50 to 22:00, and after 23:30 UTC on March 28; 01:30 to 04:30, and 06:00 to 07:59 on March 29) have fewer snowflakes per unit volume, while the average size is larger and the deviation of D_{eq} and D_{max} is larger, which may be a period when the snowflakes are sparsely distributed in space, with a high degree of aggregation of individual snowflakes and a more complex shape. On the contrary, in other periods (19:50 to 20:50 and 22:00 to 23:30 UTC on March 28; 00:00 to 01:30, and 04:30 to 06:00 on March 29), the particle counts per unit volume were smaller, while the average size and the deviation of D_{eq} and D_{max} was larger, which means the aggregation of snowflakes was weakened.

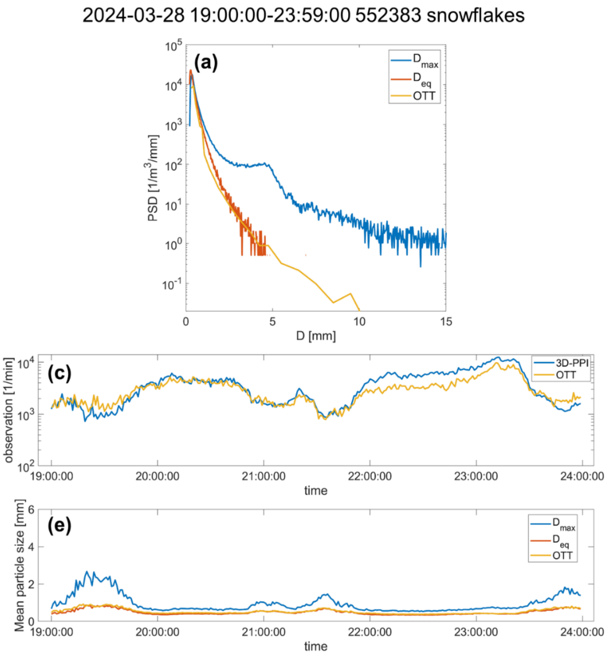

Figure 13. This typical continuous snowfall was split into two days and plotted separately (left and right). The 1-minute particle size distribution (PSD) of the D_{max} (blue) and D_{eq} (orange) for 3D-PPI and OTT (yellow) for the snowfall case (first row). Temporal plot of average particle counts per unit volume per minute over two days (second row). Temporal plot of average particle size per minute over time (third row).

5.2 Three-dimensional shape of snowflakes

Fig. 14 shows the reconstructed 3D shapes of 6 snowflakes collected on 6 April 2024. For individual snowflakes, three images were obtained from three high-resolution cameras (Cam0, Cam1, and Cam2), and the results of the 3D shape were reconstructed by utilizing the visual hull method (Fig. 14). To characterize the 3D shape of each snowflake, four parameters are calculated: volume V, maximum size D_{max} (diameter of the smallest enclosing circle), aspect ratio AR (ratio of the longest and shortest axes of the smallest outer ellipsoid), sphericity (Sp). Sp is derived from the V and S (surface area) and characterizes the degree to which 3D particles approach the sphere:

$$Sp = \frac{4\pi\left(\frac{3V}{4\pi}\right)^{\frac{2}{3}}}{S} \tag{8}$$

The 3D shapes of snowflakes ranging in volume from over 400 mm³ (Fig. 14b) to as small as less than 20 mm³ (Fig. 14f) all can be reconstructed. In the algorithm when two connected regions are close together, they are considered as the same snowflake, so the reconstructed snowflake will appear as a separated small part that is not connected to the main body, in which case D_{max} is meaningless (Fig. 14 e, f). From the results, it can be found that the visual hull approach can effectively and precisely execute the 3D reconstruction for snowflakes with highly realistic, intricate, and varied shapes and compositions, as well as diverse sizes and sphericity. The analysis of individual snowflake cases is meaningless, and here is just to show that 3D-PPI already has the capability of 3D reconstruction. Therefore, the next step is to embed the 3D reconstruction and pre-algorithms into the instrument to realize real-time, automated, and batch 3D reconstruction of snowflakes, to statistically characterize the distribution of the 3D shape of a large number of snowflakes.

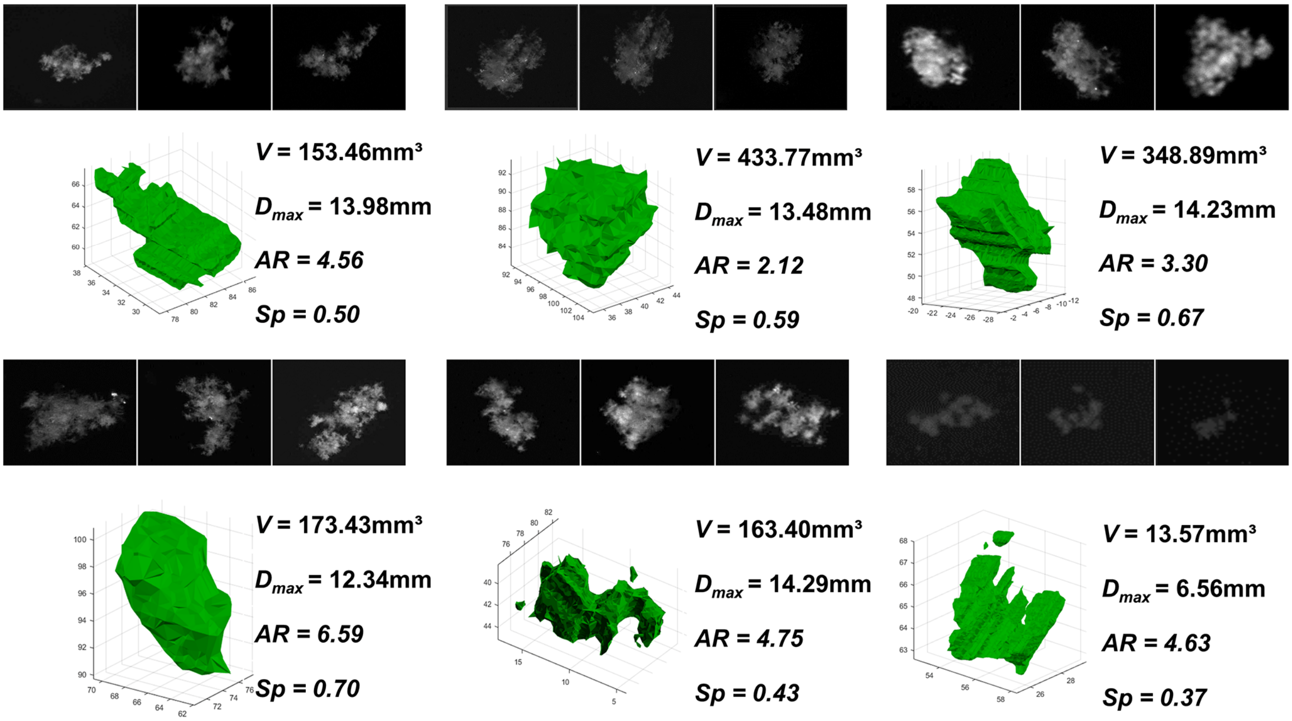

Figure 14. Several typical snowflakes captured by 3D-PPI in the field and the corresponding 3D reconstruction results. For each reconstruction, the computed V, D_{max}, AR, and Sp.

5.3 Fall velocity of snowflakes

The single exposure time of a high-speed camera is 20 µs so blurring that particle motion is insignificant, and the time between two consecutive images is 5ms. The same particle may appear in several consecutive images two or more times, and the same particle is merged into a single image in Fig. 15a, the speed calculation schematic is shown in Fig. 15b.

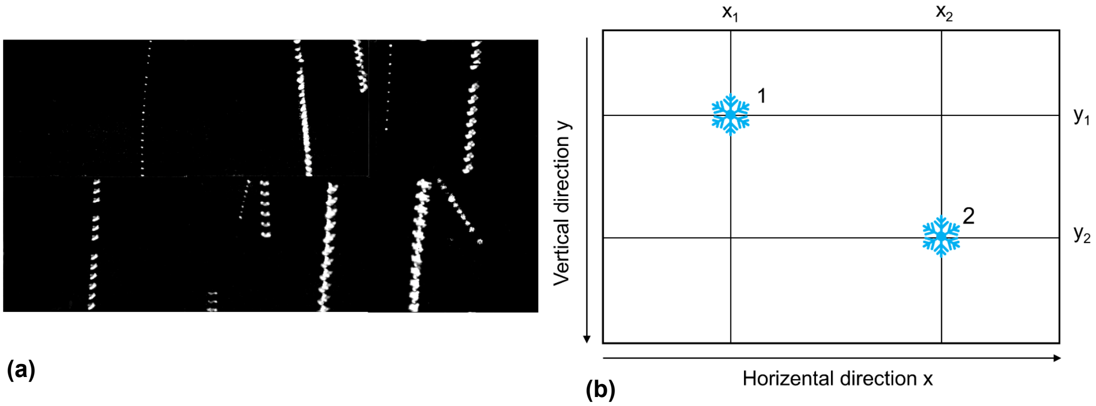

Figure 15. Processed high-speed camera images, and then the same particles are merged into a single image **(a)**. Speed Measurement Schematic **(b)**.

When there are multiple particles in a high-speed camera image, particle matching is required. The same particle is regarded as the same particle when the following three principles are satisfied: (i) the images in which the particles are located are adjacent to each other (the timestamp interval is 5ms); (ii) the pixel coordinates in the particle images are similar (the falling velocity of the snowflake is generally not more than 8m/s, so the interval between neighboring snowflakes is not more than 200 pixels); (iii) the D_{max} and D_{eq} of the particles are similar, generally not more than 20%. Each particle may have recorded anywhere from 2 to 20 D_{max}, D_{eq}, pixel horizontal coordinates, and pixel vertical coordinates. The standard deviation of D_{max}, D_{eq}, and the difference between the horizontal and vertical coordinates of each particle is calculated, and if the standard deviation of any of the particle's quantities is too large, the particle is treated to be an invalid particle, and it will be removed. D_{max} and D_{eq} of each particle are taken to be the maximum of these values, which excludes cases where the particle is not captured because it is at the edge of the image. The horizontal velocity (V_{h}) component and vertical velocity component (V_{v}) are calculated as follows:

$$V_{\mathrm{h}} = \frac{x_2 - x_1}{\Delta t} \cdot \alpha \tag{9}$$

$$V_{\mathrm{v}} = \frac{y_2 - y_1}{\Delta t} \cdot \alpha \tag{10}$$

Where, x_2, x_1 and y_2, y_1 denote the horizontal and vertical coordinates of the same particle in neighboring images; Δt denote exposure interna which is generally 5ms, but when there is a missed frame in the image to the image timestamp difference shall prevail; α denotes the magnification of the high-speed camera at the focal distance, which is 230 $\mu\mathrm{m}\cdot\mathrm{px}^{-1}$.

From 0800 UTC to 0830 UTC on 6 April 2024, the Cam3 of 3D-PPI recorded 322,267 valid snowflakes, and the snowflake velocity distribution with diameter was calculated. The horizontal velocity component and vertical velocity component are further plotted as a scatter density plot and compared to the results measured by OTT at the same period, which is shown in Fig.16. OTT's D and V binning is uneven, whereas here 3D-PPI is set to even binning with D and V intervals of

0.1mm and 0.1m/s, respectively. The red and black solid lines in Fig. 16b, d represent the empirical curves of the falling velocity and diameter of unrimed aggregates and densely rimed dendrites, respectively (Locatelli and Hobbs, 1974).

The empirical velocity of unrimed aggregates is:

$$V_1 = 0.81D^{0.16} \tag{11}$$

The empirical velocity of densely rimed dendrites is:

$$V_2 = 0.62D^{0.33} \tag{12}$$

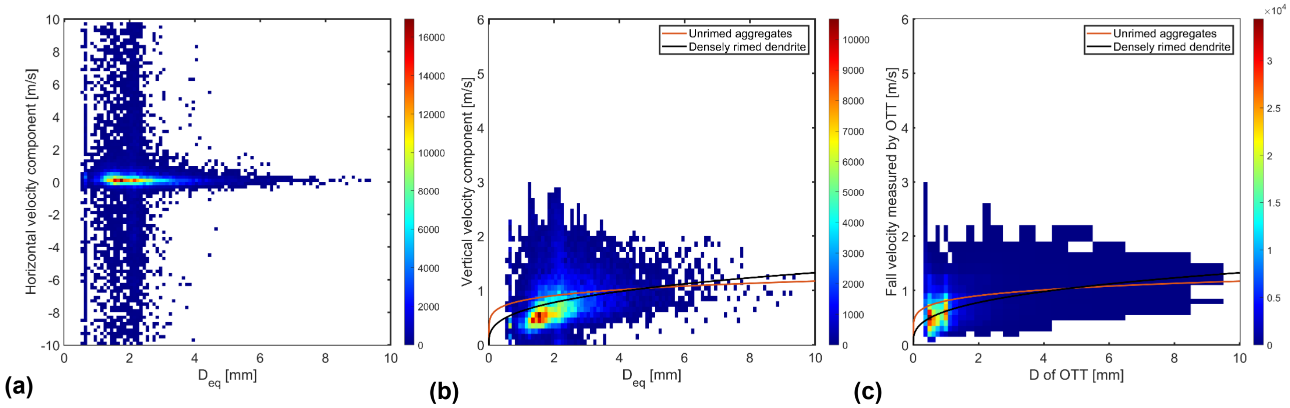

Figure 16. Distribution of horizontal **(a)**, and vertical **(b)** snowflake velocities with D$_{eq}$ measured by 3D-PPI. Distribution of falling velocity with diameter measured by OTT **(c).**

The average value of the horizontal velocity component measured by 3D-PPI is +0.05m/s (positive and negative values indicate westward and eastward velocities, respectively), and the standard deviation is 2.56m/s (Fig. 16a). The overall distribution of particle horizontal velocities ranges between ±10m/s, and more than 80% of the snowflakes have a horizontal velocity distribution between ±1.5m/s. Positive velocities predominate over negative ones, largely influenced by the prevailing westward winds. The average value of the vertical velocity component measured by 3D-PPI is 0.88m/s and the standard deviation is 0.54m/s, while, the average value and standard deviation of the velocities measured by OTT are 0.69m/s and 0.31m/s. The diameters of snowflakes measured by 3D-PPI (OTT) were concentrated in the range of 0.5 to 1.4 mm (0.4 to 1 mm). The vertical velocities were concentrated in the 0.3 to 1.2 m/s (0.3 to 0.7 m/s). The diameter and velocity values measured by 3D-PPI are larger and more dispersed than those measured by OTT. Overall the vertical velocity of snowflakes increases with the increasing diameter, and the observed data are in good agreement with the two empirical velocity relationships (Locatelli and Hobbs, 1974). It should be noted that there are a certain number of velocity outliers of snowflakes measured by the 3D-PPI, in which some large snowflakes have small velocities, and some small snowflakes have large velocities beyond empirical values.

6 Conclusion

The design of a Three-Dimensional Precipitation Particles Imager (3D-PPI) has been introduced in this paper. The 3D-PPI consists of three high-resolution cameras (4096×3000, 5fps) with telecentric lenses and one high-speed camera (720×540, 200fps) with a non-telecentric lens. Three high-resolution cameras are oriented at a 45° angle relative to the optical axis of the high-speed camera, forming an intersecting observation volume of 1505.327 cm^3. The high-resolution cameras feature a resolution of 41.5 $\mu m \cdot px^{-1}$ and are precisely synchronized by clock control which is sufficient to obtain fine shapes of snowflakes, and the large field of view of 170 mm×125 mm enables it to capture enough snowflakes to estimate PSD more accurately. The high-speed camera allows for the calculation of velocity more accurately. Besides, the utilization of telecentric lenses eliminates the sizing error caused by the uncertain distance between the snowflakes and the cameras.

For three high-resolution cameras, a calibration method using the 3D chessboard was proposed. By shooting the 3D checkerboard grid from three angles at the same time, find the correspondence between the world coordinate points and the image coordinate points and then solve the system of equations to estimate the projection matrix of the three angles. A reprojection averaging error of less than 0.4 pixels can indicate the accuracy of the calibration. Image binarization calibration is achieved by photographing ceramic reference spheres with different diameters of absolute sphericity. Both types of image processing require binarization and particle detection, and high-speed cameras require background removal, enhancement, and denoising before these two steps. The image processing algorithm needs to be evaluated by batch processing of ceramic sphere images, and the average values of the relative errors of D_{max} and D_{eq} are +2.2% and -2.7%, respectively. The issue of matching the same particle by its position in the image can be addressed by using the projection matrix obtained from the pre-calibration. The preliminary determination of the 3D spatial localization of particles after particle matching can effectively improve the computational efficiency of the 3D reconstruction algorithm, so particle localization is an indispensable step before 3D reconstruction. The snowflake 3D shape is further reconstructed using a visual hull algorithm based on binarized contour images from different angles and projection matrixes (Kleinkort et al., 2017).

The 3D-PPI was installed at Tulihe, China on January 1st, 2024, and the OTT was installed 10 meters apart for comparison. The PSDs, 3D shapes, and fall velocity of snowflakes were preliminarily analyzed. The PSD measured solely by Cam1 and that obtained by OTT exhibit excellent agreement during the typical snowfall case. Several snowflakes with different morphologies were selected and reconstructed in three dimensions, indicating that 3D-PPI is initially capable of reconstructing snowflakes. The horizontal and vertical velocities of snowflakes were calculated to obtain the velocity distribution. Further comparisons were made with the OTT, and overall, the two distributions for fall velocity were similar, however, the diameter and velocity values measured by 3D-PPI are larger and more dispersed than those measured by OTT. This difference may be attributed to the potential magnification differences of the high-speed camera in the 3D-PPI due to particles being at varying distances from the cameras.

In this paper, The PSD statistics use only one image from a high-resolution camera, and the 3D reconstruction is limited to just one case study. The next step is to optimize the 3D reconstruction algorithms of snowflakes, and statistically characterize the distribution of the 3D shape of a certain number of snowflakes. Also, the accuracy of velocity measurement still needs to be verified and improved. In the future, 3D-PPI will facilitate more precise and realistic estimations of the snowflake parameters, including the size, volume, mass, and density. Based on the above details parameters, the 3D-PPI has the potential to improve the radar-based estimation for solid precipitation in winter.

Data availability. The raw and processed 3D-PPI data mentioned in the paper are available upon request to the authors.

Author contributions. JS processed the 3D-PPI data, researched the algorithms, analyzed the data of the case, and drafted the manuscript. XL acquired funding, developed the 3D-PPI instrument, and proofread the manuscript. LL supported funding acquisition, designed the instrument, and conducted field experiments. LL contributed to instrument calibration. PW developed the hardware and software of 3D-PPI. All authors reviewed and edited the draft.

Competing interests. The authors declare that they have no conflict of interest.

Acknowledgements. Funded by the National Key Research and Development Program of China (Grant 2021YFC2802501) and National Natural Science Foundation of China (Grant No.42222505).

Appendix A: Coordinate system transformation

Camera calibration encompasses four key coordinate systems:

1. World coordinate system (WCS): Denoted as (X_w , Y_w, Z_w): This is a user-defined 3D spatial coordinate system that is utilized to describe the location of the target object within the tangible world, with units typically expressed in millimeters.
2. Camera coordinate system (CCS): Denoted as (X_c , Y_c , Z_c): This coordinate system is intrinsic to the camera and is utilized to describe the object's position relative to the camera's perspective. It acts as an intermediary between the WCS and the image (pixel) coordinate system.
3. Image coordinate system (ICS): Denoted as (x, y), this system is employed to articulate the projection and translation of the object from the CCS to the ICS during the imaging process. It facilitates the subsequent extraction of coordinates under the pixel coordinate system, with the unit being millimeters.
4. Pixel coordinate system (PCS): Denoted as (u, v), this system describes the coordinates of the object's image point post-imaging on the digital image sensor. It is the actual coordinate system from which image information is read from the camera, measured in units of pixels.

The camera imaging process involves the transformation from WCS to PCS. Camera calibration, in essence, is the procedure of determining the transformation relationships between these four coordinate systems.

A.1 WCS to CCS

Firstly, the transformation of a camera shot from the WCS to the CCS is a rigid-body transformation, where the object does not deform, but only rotates and translates. Only the rotation matrix R and translation matrix T need to be obtained. The camera coordinate system is obtained by rotating θ, α, and β angles around the z, y, and x-axes in turn and translating to obtain the rotation matrix in the three dimensions:

$$R_z(\theta)=\begin{bmatrix}\cos(\theta) & \sin(\theta) & 0\\ -\sin(\theta) & \cos(\theta) & 0\\ 0 & 0 & 1\end{bmatrix}$$
$$R_y(\beta)=\begin{bmatrix}\cos(\beta) & 0 & -\sin(\beta)\\ 0 & 1 & 0\\ \sin(\beta) & 0 & \cos(\beta)\end{bmatrix} \qquad (\text{A.1})$$
$$R_x(\alpha)=\begin{bmatrix}1 & 0 & 0\\ 0 & \cos(\alpha) & \sin(\alpha)\\ 0 & -\sin(\alpha) & \cos(\alpha)\end{bmatrix}$$

The three matrices are multiplied together to obtain a three-dimensional rotation matrix:

$$R=R_x(\alpha)R_y(\beta)R_z(\theta)=$$
$$\begin{bmatrix}\cos(\beta)\cos(\theta) & \cos(\beta)\sin(\theta) & -\sin(\beta)\\ -\cos(\alpha)\sin(\theta)+\sin(\alpha)\sin(\beta)\cos(\theta) & \cos(\alpha)\cos(\theta)+\sin(\alpha)\sin(\beta)\sin(\theta) & \sin(\alpha)\cos(\beta)\\ \sin(\alpha)\sin(\theta)+\cos(\alpha)\sin(\beta)\cos(\theta) & -\sin(\alpha)\cos(\theta)+\cos(\alpha)\sin(\beta)\sin(\theta) & \cos(\alpha)\cos(\beta)\end{bmatrix} \qquad (\text{A.2})$$

Where, for z, y, and x direction of rotation is followed by the right-hand spiral rule, the thumb points to the direction of the axis, and the four-finger direction is the positive direction of rotation.

For the translation matrix, at this point, the coordinates are already in the same direction as CCS, but with the world coordinate system origin coinciding with the coordinates under the coordinates, converting the camera coordinate system also needs to be added to the translation is WCS origin in CCS under the coordinates T.

The rotation and translation process can be expressed by the formula:

$$\begin{bmatrix}X_c\\ Y_c\\ Z_c\\ 1\end{bmatrix}=\begin{bmatrix}R_{3\times3} & T_{3\times1}\\ O & 1\end{bmatrix}\cdot\begin{bmatrix}X_w\\ Y_w\\ Z_w\\ 1\end{bmatrix} \qquad (\text{A.3})$$

A.2 CCS to ICS

The difference between telecentric cameras and traditional pinhole cameras is the difference in projection. A pinhole camera uses a perspective projection to transform from CCS to ICS; a telecentric camera uses an orthogonal projection. The relationship between CCS and ICS is as follows:

$$\begin{bmatrix}x\\ y\\ 1\end{bmatrix}=\begin{bmatrix}\beta & 0 & 0 & 0\\ 0 & \beta & 0 & 0\\ 0 & 0 & 0 & 1\end{bmatrix}\cdot\begin{bmatrix}X_c\\ Y_c\\ Z_c\\ 1\end{bmatrix} \qquad (\text{A.4})$$

where β is the magnification of the telecentric lens of the telecentric camera. It is not difficult to see that the image coordinates are independent of the camera coordinates Z_c, i.e. the distance of the object to be photographed from the lens does not affect the imaging (projection) of the image, which is also in line with the characteristics of telecentric lens imaging.

A.3 ICS to PCS

To convert a point in ICS whose origin is at the center of the light in real physical units to a point in an image coordinate system whose origin is at the top left corner of pixels requires two transformations, translation, and scaling, which are affine transformations.

$$\begin{bmatrix} u \\ v \\ 1 \end{bmatrix} = \begin{bmatrix} \frac{1}{S_u} & 0 & u_0 \\ 0 & \frac{1}{S_v} & v_0 \\ 0 & 0 & 1 \end{bmatrix} \begin{bmatrix} x \\ y \\ 1 \end{bmatrix} \tag{A.5}$$

where the pixel size is $S_u \times S_v$, (u_0, v_0) is the pixel coordinate of the optical center point.

A.4 WCS to PCS

Integration of expressions from the first three sections:

$$\begin{aligned} \begin{bmatrix} u \\ v \\ 1 \end{bmatrix} &= \begin{bmatrix} \frac{1}{S_u} & 0 & u_0 \\ 0 & \frac{1}{S_v} & v_0 \\ 0 & 0 & 1 \end{bmatrix} \cdot \begin{bmatrix} \beta & 0 & 0 & 0 \\ 0 & \beta & 0 & 0 \\ 0 & 0 & 0 & 1 \end{bmatrix} \cdot \begin{bmatrix} r_{11} & r_{12} & r_{13} & t_x \\ r_{21} & r_{22} & r_{23} & t_y \\ r_{31} & r_{32} & r_{33} & t_z \\ 0 & 0 & 0 & 1 \end{bmatrix} \cdot \begin{bmatrix} X_w \\ Y_w \\ Z_w \\ 1 \end{bmatrix} \\ &= \begin{bmatrix} \frac{\beta}{S_u} & 0 & u_0 \\ 0 & \frac{\beta}{S_v} & v_0 \\ 0 & 0 & 1 \end{bmatrix} \cdot \begin{bmatrix} r_{11} & r_{12} & r_{13} & t_x \\ r_{21} & r_{22} & r_{23} & t_y \\ 0 & 0 & 0 & 1 \end{bmatrix} \cdot \begin{bmatrix} X_w \\ Y_w \\ Z_w \\ 1 \end{bmatrix} \end{aligned} \tag{A.6}$$

Similar to small hole imaging, $\begin{bmatrix} \frac{\beta}{S_u} & 0 & u_0 \\ 0 & \frac{\beta}{S_v} & v_0 \\ 0 & 0 & 1 \end{bmatrix}$ is the internal parameter of the camera, which only relates to the camera itself and has nothing to do with the position of the camera. $\begin{bmatrix} r_{11} & r_{12} & r_{13} & t_x \\ r_{21} & r_{22} & r_{23} & t_y \\ 0 & 0 & 0 & 1 \end{bmatrix}$ is an external parameter of the camera, representing the position of the camera. It has nothing to do with camera manufacturing or lens distortion, but only with the mounting position and angle of the camera in WCS. R and T represent the rotation and translation process from WCS to CCS, respectively. Compared to common pinhole lenses, the four quantities r_{31}, r_{32}, r_{33}, and t_z in the third row of the external reference matrix of the telecentric camera do not exist. This further confirms the special feature of telecentric camera imaging, i.e. it is a parallel light projection and the distance of the object from the camera does not affect the size of the object in the image.

References

Bailey, M. and Hallett, J.: Ice Crystal Linear Growth Rates from −20° to −70°C: Confirmation from Wave Cloud Studies, J. Atmos. Sci., 69, 390-402, https://doi.org/10.1175/jas-d-11-035.1, 2012.

Battaglia, A., Rustemeier, E., Tokay, A., Blahak, U., and Simmer, C.: PARSIVEL Snow Observations: A Critical Assessment J. Atmos. Ocean. Tech., 27, 333-344, https://doi.org/10.1175/2009jtecha1332.1, 2010.

Bernauer, F., Hürkamp, K., Rühm, W., and Tschiersch, J.: Snow event classification with a 2D video disdrometer — A decision tree approach, Atmos. Res., 172-173, 186-195, https://doi.org/10.1016/j.atmosres.2016.01.001, 2016.

Cheng, Q. and Huang, P.: Camera Calibration Based on Phase Estimation, IEEE Trans. Instrum. Meas., 72, 1-9, https://doi.org/10.1109/tim.2022.3227554, 2023.

Garrett, T. J., Fallgatter, C., Shkurko, K., and Howlett, D.: Fall speed measurement and high-resolution multi-angle photography of hydrometeors in free fall, Atmos. Meas. Tech., 5, 2625-2633, https://doi.org/10.5194/amt-5-2625-2012, 2012.

Gergely, M. and Garrett, T. J.: Impact of the natural variability in snowflake diameter, aspect ratio, and orientation on modeled snowfall radar reflectivity J. Geophys. Res.: Atmos., 121, 12236-12252, https://doi.org/10.1002/2016jd025192, 2016.

Hauswiesner, S., Straka, M., and Reitmayr, G.: Temporal coherence in image-based visual hull rendering, IEEE Trans. Visual Comput. Graphics, Vol.19, 1758-1767, https://doi.org/10.1109/tvcg.2013.85, 2013.

Helms, C. N., Munchak, S. J., Tokay, A., and Pettersen, C.: A comparative evaluation of snowflake particle shape estimation techniques used by the Precipitation Imaging Package (PIP), Multi-Angle Snowflake Camera (MASC), and Two-Dimensional Video Disdrometer (2DVD), Atmos. Meas. Tech., 15, 6545-6561, https://doi.org/10.5194/amt-15-6545-2022, 2022.

Kim, M.-J., Kulie, M. S., O'Dell, C., and Bennartz, R.: Scattering of Ice Particles at Microwave Frequencies: A Physically Based Parameterization, J. Appl. Meteor. Climatol., 46, 615-633, https://doi.org/10.1175/jam2483.1, 2007.

Kim, M. J.: Single scattering parameters of randomly oriented snow particles at microwave frequencies, J. Geophys. Res.: Atmos., 111, https://doi.org/10.1029/2005jd006892, 2006.

Kleinkort, C., Huang, G. J., Bringi, V. N., and Notaroš, B. M.: Visual Hull Method for Realistic 3D Particle Shape Reconstruction Based on High-Resolution Photographs of Snowflakes in Free Fall from Multiple Views, J. Atmos. Ocean. Tech., 34, 679-702, https://doi.org/10.1175/jtech-d-16-0099.1, 2017.

Kneifel, S., Löhnert, U., Battaglia, A., Crewell, S., and Siebler, D.: Snow scattering signals in ground‐based passive microwave radiometer measurements, J. Geophys. Res.: Atmos., 115, https://doi.org/10.1029/2010jd013856, 2010.

Liu, X., He, B., Zhao, S., Hu, S., and Liu, L.: Comparative measurement of rainfall with a precipitation micro-physical characteristics sensor, a 2D video disdrometer, an OTT PARSIVEL disdrometer, and a rain gauge, Atmos. Res., 229, 100-114, https://doi.org/10.1016/j.atmosres.2019.06.020, 2019.

Liu, X. C., Gao, T. C., and Liu, L.: A video precipitation sensor for imaging and velocimetry of hydrometeors, Atmos. Meas. Tech., 7, 2037-2046, https://doi.org/10.5194/amt-7-2037-2014, 2014.

Locatelli, J. D. and Hobbs, P. V.: Fall speeds and masses of solid precipitation particles J. Geophys. Res, 79, 2185-2197, https://doi.org/10.1029/JC079i015p02185, 1974.

Loffler-Mang, M. and Joss, J.: An Optical Disdrometer for Measuring Size and Velocity of Hydrometeors J. Atmos. Ocean. Tech., 17, 130-139, https://doi.org/10.1175/1520-0426(2000)017<0130:Aodfms>2.0.Co;2, 2000.

Maahn, M., Moisseev, D., Steinke, I., Maherndl, N., and Shupe, M. D.: Introducing the Video In Situ Snowfall Sensor (VISSS), Atmos. Meas. Tech., 17, 899-919, https://doi.org/10.5194/amt-17-899-2024, 2024.

Mason, S. L., Hogan, R. J., Westbrook, C. D., Kneifel, S., Moisseev, D., and von Terzi, L.: The importance of particle size distribution and internal structure for triple-frequency radar retrievals of the morphology of snow, Atmos. Meas. Tech., 12, 4993-5018, https://doi.org/10.5194/amt-12-4993-2019, 2019.

Minda, H., Tsuda, N., and Fujiyoshi, Y.: Three-Dimensional Shape and Fall Velocity Measurements of Snowflakes Using a Multiangle Snowflake Imager, J. Atmos. Ocean. Tech., 34, 1763-1781, https://doi.org/10.1175/jtech-d-16-0221.1, 2017.

https://doi.org/10.5194/amt-2024-106
Preprint. Discussion started: 12 July 2024

Morrison, H., van Lier‐Walqui, M., Fridlind, A. M., Grabowski, W. W., Harrington, J. Y., Hoose, C., Korolev, A., Kumjian, M. R., Milbrandt, J. A., Pawlowska, H., Posselt, D. J., Prat, O. P., Reimel, K. J., Shima, S. I., van Diedenhoven, B., and Xue, L.: Confronting the Challenge of Modeling Cloud and Precipitation Microphysics, J. Adv. Model. Earth Syst., 12, https://doi.org/10.1029/2019ms001689, 2020.

Newman, A. J., Kucera, P. A., and Bliven, L. F.: Presenting the Snowflake Video Imager (SVI), J. Atmos. Ocean. Tech., 26, 167-179, https://doi.org/https://doi.org/10.1175/2008JTECHA1148.1, 2009.

Notaroš, B., Bringi, V., Kleinkort, C., Kennedy, P., Huang, G.-J., Thurai, M., Newman, A., Bang, W., and Lee, G.: Accurate Characterization of Winter Precipitation Using Multi-Angle Snowflake Camera, Visual Hull, Advanced Scattering Methods and Polarimetric Radar, Atmosphere, 7, https://doi.org/10.3390/atmos7060081, 2016.

Olson, W. S., Tian, L., Grecu, M., Kuo, K.-S., Johnson, B. T., Heymsfield, A. J., Bansemer, A., Heymsfield, G. M., Wang, J. R., and Meneghini, R.: The Microwave Radiative Properties of Falling Snow Derived from Nonspherical Ice Particle Models. Part II: Initial Testing Using Radar, Radiometer and In Situ Observations, J. Appl. Meteor. Climatol., 55, 709-722, https://doi.org/10.1175/jamc-d-15-0131.1, 2016.

Pettersen, C., Bliven, L. F., von Lerber, A., Wood, N. B., Kulie, M. S., Mateling, M. E., Moisseev, D. N., Munchak, S. J., Petersen, W. A., and Wolff, D. B.: The Precipitation Imaging Package: Assessment of Microphysical and Bulk Characteristics of Snow, Atmosphere, 11, 785, https://doi.org/10.3390/atmos11080785, 2020a.

Pettersen, C., Bliven, L. F., von Lerber, A., Wood, N. B., Kulie, M. S., Mateling, M. E., Moisseev, D. N., Munchak, S. J., Petersen, W. A., and Wolff, D. B.: The Precipitation Imaging Package: Assessment of Microphysical and Bulk Characteristics of Snow, Atmosphere, 11, https://doi.org/10.3390/atmos11080785, 2020b.

Taylor, P. a.: H. R. Pruppacher and J. D. Klett, Microphysics of Clouds and Precipitation, Boundary-Layer Meteorol., 86, 187-188, https://doi.org/10.1023/a:1000652616430, 1998.

Tyynelä, J., Leinonen, J., Moisseev, D., and Nousiainen, T.: Radar Backscattering from Snowflakes: Comparison of Fractal, Aggregate, and Soft Spheroid Models, J. Atmos. Ocean. Tech., 28, 1365-1372, https://doi.org/10.1175/jtech-d-11-00004.1, 2011.

Zhang, Y., Zhang, L., Lei, H., Xie, Y., Wen, L., Yang, J., and Wu, Z.: Characteristics of Summer Season Raindrop Size Distribution in Three Typical Regions of Western Pacific J. Geophys. Res.: Atmos., 124, 4054-4073, https://doi.org/10.1029/2018jd029194, 2019.